JOURNAL OF GUIDANCE, CONTROL, AND DYNAMICS
Vol. 33, No. 1, January–February 2010

Autonomous Navigation in Three-Dimensional Urban Environments Using Wide-Field Integration of Optic Flow

Andrew M. Hyslop* and J. Sean Humbert†
University of Maryland, College Park, Maryland 20742

DOI: 10.2514/1.43778

In this paper, a control theoretic framework is introduced to analyze an information extraction approach from patterns of optic flow based on analogs to wide-field motion-sensitive interneurons in the insect visuomotor system. An algebraic model of optic flow is developed, based on a parameterization of three-dimensional urban environments. It is shown that estimates of proximity and speed, relative to these environments, can be extracted using weighted summations of the instantaneous patterns of optic flow. Small perturbation techniques are then applied to link weighting patterns to outputs, which are applied as feedback to facilitate stability augmentation and perform local obstacle avoidance and terrain following. Additive noise and environment uncertainties are incorporated into an offline procedure for determination of optimal weighting functions. Stability is proven via local asymptotic analysis and the resulting approach demonstrated in simulation using a micro helicopter in a three-dimensional urbanlike environment.

Nomenclature

A = state-space dynamics matrix
a = tunnel half-width or distance to obstacle, m
B = control coefficient matrix
$\mathcal{B}$ = body frame
C = observation matrix
$C^{\dagger}$ = observation inversion matrix
c = cosine function
d = distance, m
$\mathbf{F}$ = weighting/basis function
$\mathcal{F}$ = inertial fixed frame
g = distance to front/rear obstacle, m
h = nominal height above ground, m
J = linear quadratic regulation performance index
K = gain matrix
M = number of spherical harmonic outputs
n = number of optic-flow-encoded states
P = state estimate covariance matrix
p = roll rate, rad/s
$\mathbf{Q}$ = optic flow
$\mathbf{q}$ = vehicle pose
q = pitch rate, rad/s
R = noise covariance matrix
$\mathcal{R}$ = rotation matrix
$\mathbf{r}$ = point on a spherical imaging surface
r = yaw rate, rad/s
s = sine function
$\mathbf{u}$ = control vector
u = forward velocity, m/s
$\mathbf{v}$ = velocity vector, m/s
v = lateral velocity, m/s
W = output weighting matrix
$\mathbf{w}$ = wide-field integration measurement noise vector
w = vertical velocity, m/s
$\mathbf{x}$ = vehicle state vector
x = forward distance, m
$\hat{\mathbf{x}}$ = static state estimates
Y = spherical harmonic function
$\mathbf{y}$ = wide-field integration outputs, rad/s
y = lateral distance, m
z = vertical distance, m
β = body-referred elevation angle, rad
γ = body-referred azimuth angle, rad
δ = perturbation
ε = uncertainty relative weighting
$\boldsymbol{\eta}$ = optic flow measurement noise vector
θ = pitch angle, rad
Λ = normalized actuator input
μ = nearness function, 1/m
ξ = lateral flapping angle, rad
Φ = Legendre function
ϕ = roll angle, rad
χ = longitudinal flapping angle, rad
ψ = heading angle, rad
Ω = solid angle, sr
$\boldsymbol{\omega}$ = angular rate vector, rad/s

Subscripts and Superscripts

b = body frame
cl = closed loop
D = inertial down direction
E = inertial east
l = harmonic degree
lat = lateral
lon = longitudinal
N = inertial north
m = harmonic order
mr = main rotor
ref = instantaneous reference/target trajectory
S = inertial south
t = thrust

Presented as Paper 7252 at the AIAA Guidance, Navigation, and Control Conference, Honolulu, HI, 19–23 August 2008; received 12 February 2009; revision received 21 August 2009; accepted for publication 26 September 2009.

*Ph.D. Student, Department of Aerospace Engineering; ahyslop@umd.edu. Student Member AIAA.

†Assistant Professor, Department of Aerospace Engineering, 3182 Martin Hall; humbert@umd.edu. Senior Member AIAA.

U = inertial up direction
W = inertial west
0 = nominal
$\tilde{}$ = measured quantity
$\hat{}$ = estimated quantity

I. Introduction

INTEREST in micro air vehicle (MAV) platforms has expanded significantly in recent years, primarily due to the requirement for inexpensive surveillance and reconnaissance. To be truly effective, these platforms will need to be endowed with the capability to operate autonomously in the environments of interest. Existing guidance systems consistent with MAV payloads are bandwidth limited (5 Hz), weigh on the order of 15–30 g, require 0.75–1 W of power, and do not function indoors due to global positioning system availability. Miniature laser rangefinders and ultrasonics have the required bandwidth; however, implementations are also on the order of 25–40 g, require 400 mW, and have a very limited field of view. Traditional machine vision approaches [1–6] that infer proximity and velocity information from camera imagery have been demonstrated; however, these algorithms are computationally expensive and require offboard visual processing, even on vehicles with significant payloads [7]. For an aerial microsystem with a requirement of both indoor and outdoor operation, there are currently no viable approaches to achieve the required velocity estimation, obstacle localization, and avoidance. Hence, novel sensors and sensory processing architectures will need to be explored if autonomous microsystems are to be ultimately successful.

For inspiration, researchers are looking to the millions of examples of flying insects that have developed elegant solutions to the challenges of visual perception and navigation [8]. Insects rely on optic flow [9,10], the characteristic patterns of visual motion that form on their retinas as they move. These time-dependent motion patterns are a rich source of visual cues that are a function of the relative velocity and proximity of the insect with respect to obstacles in the surrounding environment [11]. The discovery of common navigational heuristics [12–14] observed in behavioral experiments with animals has spawned several biologically inspired approaches for MAV navigation. Recent efforts include obstacle centering [15,16], avoidance [17–19], and terrain following [20–22]. In most of these cases, a feedback signal is generated by comparing single points or uniformly averaged patches of optic flow on the sides or the bottom of a vehicle to generate either continuous control input, intermittent avoidance maneuvers, or both. Some studies require independent sensing of vehicle rotation rates, and results are predominately presented without formal closed-loop stability analysis. Additionally, the previously mentioned approaches ignore (in favor of more traditional architectures) the fundamental processing and feedback mechanisms that insects employ to extract information from optic flow and to regulate behavior.

In other studies, algorithms have been applied to generate estimates of egomotion and/or the structure of objects in the surrounding environment based on optic flow measurements. Past research has typically fitted a theoretical model of optic flow to measurements at a series of points in an image by numerical solution of the least-squares problem [23–26]. This procedure can be used to extract the direction of a vehicle's velocity vector as well as its rotation rates. Alternatively, one can solve for the vehicle motion states using an estimate of the terrain shape and subsequently use the egomotion to refine the terrain shape estimate [23,27]. Noise robustness was accounted for in [28], using a bioinspired approach to measure motion states, but the study did not close the control loop or extend to obstacle avoidance. Motion extraction can also be achieved using extended Kalman filters, with the nonlinear optic flow equations forming the measurement model [2,29,30]. Kalman filtering finds additional use in smoothing noisy state estimates obtained from least-squares solvers [23]. However, these studies do not address obstacle avoidance, and an accurate vehicle/environment model is usually required [23,24,27]. The associated computational burden is high, especially for algorithms that employ a feature tracking step to select high contrast image points at which optic flow can be more accurately measured [24,27,30,31].

In the majority of flying insects, specialized neurons called tangential cells, which are responsive to wide-field patterns of retinal motion, parse complex optic flow patterns over large swaths of the visual field to extract cues for navigation [32–34]. The autonomous vehicle laboratory (AVL) at the University of Maryland has developed a framework to analyze this unique information extraction approach, termed wide-field integration (WFI) [35]. The concept is based on static feedback that generates compensatory commands to hold simple patterns of optic flow fixed on an imaging surface, such as the typical sine wave pattern induced on a circular sensor by forward motion in a corridor. Weighted summations of optic flow measurements are used to detect spatial imbalances, shifts, and magnitude changes that have interpretations of relative proximity and speed with respect to objects in the surrounding environment. An example of this approach has been observed in the landing behavior of honeybees; a simple feedback loop that holds the ratio of forward speed to height constant while descending toward a surface guarantees an exponentially decaying approach trajectory [36], without the knowledge of absolute speed or distance. Complicated patterns of optic flow can therefore be rapidly decomposed into compensatory motor commands that maneuver the vehicle safely between obstacles [35,37–39].

The primary advantage of WFI is computational simplicity; it does not require direct vehicle state estimation, visual feature detection, extraction, or classification. Useful information for stability augmentation and navigation is obtained by analogs to tangential cell processing (i.e., computing a handful of inner products of optic flow). This is a very efficient process that is extremely robust to noise and does not require high resolution visual imagery. It has been recently demonstrated that this approach can be implemented in real time in analog VLSI (very large-scale integration) at a high bandwidth (1 KHz), using basic Reichardt-type elementary motion detectors for optic flow estimation and a programmable current matrix for computing inner products of optic flow measurements [40]. These sensors consume power on the order of microwatts, and can be packaged on the order of milligrams. Therefore, WFI offers orders of magnitude improvement in bandwidth, power consumption, and payload weight over implementations of traditional methodologies described previously, which are constrained to operate on digital processors. The objective of this paper is to extend WFI methods to a 6-DOF rotary wing MAV and demonstrate simultaneous flight stabilization and obstacle avoidance with proportional feedback of weighted two-dimensional (2-D) optic flow measurements.

The paper is outlined as follows. In Sec. II, a framework for the analysis of spatial decompositions of optic flow patterns on spherical imaging surfaces is developed. An offline procedure for determination of optimal weighting patterns for static estimation of relative states that account for noise and environmental uncertainty is presented in Sec. III. Section IV introduces a static feedback approach for flight stabilization and relative navigation, which is validated in simulations of a rotary wing MAV within a three-dimensional (3-D) urban environment in Sec. V. Feasibility of the resulting approach is discussed in Sec. VI, along with comparisons with existing navigation methodologies.

II. Wide-Field Integration of Optic Flow

In this section, an inner product model for tangential cell analogs is presented, and the WFI framework is introduced to characterize the information that can be extracted from patterns of optic flow on spherical imaging surfaces. An algebraic model of optic flow is developed based on a parameterization of the family of expected 3-D environments. Small perturbation techniques are then applied to link weighting patterns to outputs, which are functions of relative proximity and velocity with respect to the parameterized environments.

A. Optic Flow Model

The (true) optic flow is the vector field of relative velocities of material points in the environment projected into the tangent space of

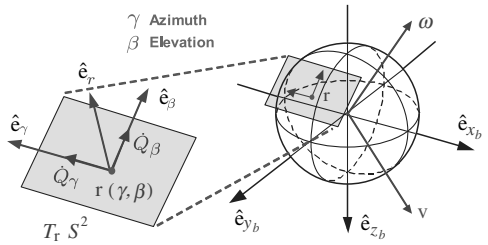

Fig. 1 Geometry for spherical optic flow. Optic flow is the projected relative velocities of the objects in the environment into the tangent space $T_r S^2$ of the imaging surface: a sphere.

the imaging surface (Fig. 1). It is a combination of the observer's rotational and translational motion, along with the relative proximity to surrounding objects. For a given angular velocity $\boldsymbol{\omega}$ and translational velocity $\mathbf{v}$ of the vantage point, along with the nearness function μ (which represents the distribution of objects in the surrounding environment), the optic flow pattern $\dot{\mathbf{Q}}$ on a spherical imaging surface S^2 for an arbitrary distribution of obstacles can be expressed [41] as

$$\dot{\mathbf{Q}} = -\boldsymbol{\omega} \times \mathbf{r} - \mu[\mathbf{v} - \langle \mathbf{v}, \mathbf{r} \rangle \mathbf{r}] \tag{1}$$

The quantity $\dot{\mathbf{Q}} = \dot{Q}_\gamma \hat{\mathbf{e}}_\gamma + \dot{Q}_\beta \hat{\mathbf{e}}_\beta$ has components in the azimuth γ and elevation β directions (Fig. 1) and lives in the vector-valued space of square-integrable functions on the sphere:

$$L^2(S^2, \mathbb{R}^2) = \left\{ \mathbf{f} = \begin{bmatrix} f_1(\mathbf{r}) \\ f_2(\mathbf{r}) \end{bmatrix} : \mathbf{r} \in S^2, f_k(\mathbf{r}) \in L^2(S^2), k = 1, 2 \right\} \tag{2}$$

If one expresses the velocity $\mathbf{v} = (u, v, w)$ and the angular velocity $\boldsymbol{\omega} = (p, q, r)$ in coordinates of the body frame $\mathcal{B} = \{\hat{\mathbf{e}}_{x_b}, \hat{\mathbf{e}}_{y_b}, \hat{\mathbf{e}}_{z_b}\}$, the expressions for the azimuthal and elevation components of optic flow are given by

$$\begin{aligned} \dot{Q}_\gamma &= p \cos\beta \cos\gamma + q \cos\beta \sin\gamma - r \sin\beta \\ &\quad + \mu(u \sin\gamma - v \cos\gamma) \\ \dot{Q}_\beta &= p \sin\gamma - q \cos\gamma + \mu(-u \cos\beta \cos\gamma \\ &\quad - v \cos\beta \sin\gamma + w \sin\beta) \end{aligned} \tag{3}$$

B. Parameterization of the Environment

To completely specify the optic flow pattern in Eq. (3) in closed form, simplifying assumptions are required on the shape of the nearness function $\mu(\gamma, \beta, \mathbf{q}) \in L^2(S^2)$. The nearness function is equal to $1/d(\gamma, \beta, \mathbf{q})$, where $d(\gamma, \beta, \mathbf{q}) \in (0, \infty)$ is the distance from the imaging surface to the nearest object in the environment, along the direction $\hat{\mathbf{e}}_r$ (Fig. 2b), and through a point on the imaging surface $\mathbf{r} = (\gamma, \beta)$. This function encodes the vehicle's relative pose $\mathbf{q} = (x, y, z, \phi, \theta, \psi)$ with respect to the environment, where (x, y, z) are the coordinates of the vantage point with respect to an inertial frame $\mathcal{F} = \{\hat{\mathbf{e}}_x, \hat{\mathbf{e}}_y, \hat{\mathbf{e}}_z\}$ located at the equilibrium position, and (ψ, θ, ϕ) are the 3-2-1 Euler angles, representing the relative attitude of the body frame $\mathcal{B}$ with respect to $\mathcal{F}$.

If the environment is assumed to be an enclosed rectangular prism (Fig. 2a), the nearness $\mu(\gamma, \beta, \mathbf{q})$ is a piecewise continuous function given by

$$\mu(\gamma, \beta, \mathbf{q}) = \begin{cases} \dfrac{s\beta[c\psi c\theta c\gamma + s\gamma(s\phi s\theta - c\phi s\psi c\theta)] + c\beta(s\phi s\psi c\theta + c\phi s\theta)}{g_N - x} & \text{front wall} \\ -\dfrac{s\beta(c\psi c\theta c\gamma + s\gamma[s\phi s\theta - c\phi s\psi c\theta)] + c\beta(s\phi s\psi c\theta + c\phi s\theta)}{g_S + x} & \text{rear wall} \\ \dfrac{s\beta(c\gamma c\theta s\psi + s\gamma[s\phi s\theta s\psi + c\phi c\psi)] + c\beta(c\phi s\theta s\psi - s\phi c\psi)}{a_E - y} & \text{right wall} \\ -\dfrac{s\beta(c\gamma c\theta s\psi + s\gamma[s\phi s\theta s\psi + c\phi c\psi)] + c\beta(c\phi s\theta s\psi - s\phi c\psi)}{a_W + y} & \text{left wall} \\ \dfrac{s\beta(s\phi c\theta s\gamma - s\theta c\gamma) + c\beta c\phi c\theta}{h_D - z} & \text{ground} \\ -\dfrac{s\beta(s\phi c\theta s\gamma - s\theta c\gamma) + c\beta c\phi c\theta}{h_U + z} & \text{ceiling} \end{cases} \tag{4}$$

Parameters $(g_N, g_S, a_E, a_W, h_D, h_U)$ represent the desired distance from the walls at the equilibrium position. The derivation for Eq. (4) is presented in Appendix B. The bounds for the validity ranges of each μ subfunction specify where the surfaces intersect, but due to their complexity, they can only be computed numerically. Analysis in the following sections is performed using numerical values for the validity bounds.

The indoorlike environment described by Eq. (4) can be simplified to environments useful for outdoor navigation. Flight above a flat surface with no obstacles is modeled by the case for which $(g_N, g_S, a_E, a_W, h_U) \to \infty$ (Fig. 2b). If there is an east-side obstacle, then $(g_N, g_S, a_W, h_U) \to \infty$ (in which Fig. 3b shows the

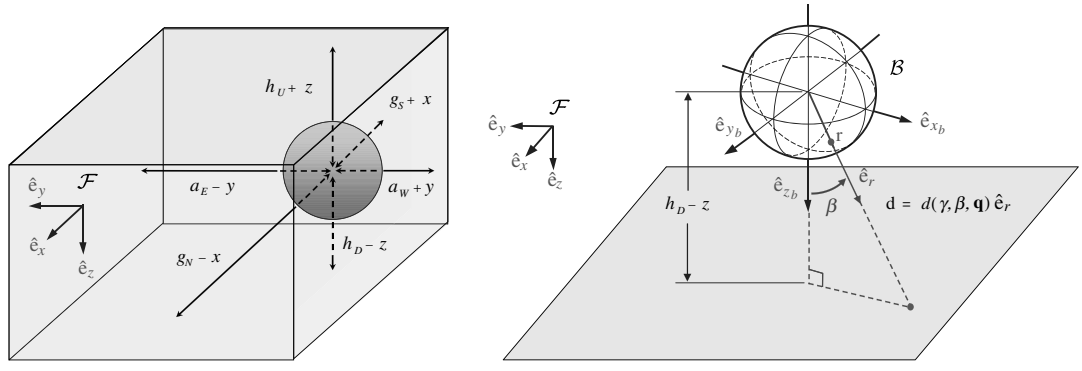

a) b)

Fig. 2 Environment models for nearness function approximation: a) enclosed room with translational perturbations; and b) flat terrain and definition of the distance function $d(\gamma, \beta, \mathbf{q})$.

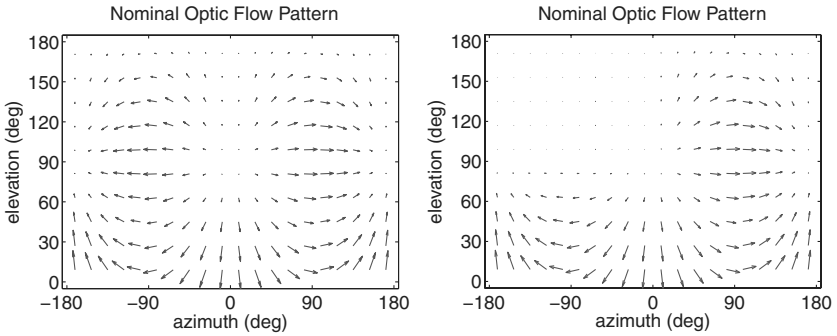

a) b)

Fig. 3 Nominal optic flow patterns: a) tunnel with floor; and b) right wall with floor.

expected optic flow pattern for straight and level flight). For a west-side obstacle, $(g_N, g_S, a_E, h_U) \to \infty$, and for the case in which there are obstacles on both sides of the vehicle, $(g_N, g_S, h_U) \to \infty$ and $a_E = a_W$ (Fig. 3a).

C. Tangential Cell Analogs

Tangential cells are large, motion-sensitive neurons that reside in the visuomotor systems of most flying insects. They are believed to pool the outputs of large numbers of local optic flow estimates and respond with graded membrane potentials, for which the magnitude is both spatially and directionally selective [9,10,42,43]. Essentially, the integrated output is a comparison between the cell's spatial sensitivity pattern and that of the visual stimulus (e.g., Fig. 3). Mathematically, this comparison can be modeled as an inner product $\langle \mathbf{a}, \mathbf{b} \rangle$, analogous with the dot product between vectors, which is an abstraction of the angle between objects **a** and **b**. Tangential cell analogs for spherical imaging surfaces are defined as the inner product on the function space $L^2(S^2, \mathbb{R}^2)$ between the instantaneous optic flow $\dot{\mathbf{Q}}$ and any square-integrable weighting function $\mathbf{F} = F^\gamma \hat{\mathbf{e}}_\gamma + F^\beta \hat{\mathbf{e}}_\beta$:

$$\langle \dot{\mathbf{Q}}, \mathbf{F} \rangle = \int_{S^2} \dot{\mathbf{Q}} \cdot \mathbf{F} \, \mathrm{d}\Omega \tag{5}$$

where $\cdot$ denotes the dot product in $\mathbb{R}^2$, and $\mathrm{d}\Omega = \sin\beta \, \mathrm{d}\beta \, \mathrm{d}\gamma$ is the solid angle of the sphere.

Real spherical harmonics (Fig. 4), which are orthogonal functions on $L^2(S^2)$, will be used as weighting functions in the two component directions (γ, β) to extract desired information from Eq. (3). These functions take the form:

$$Y_{l,m}(\beta, \gamma) = N_l^m \Phi_l^m(\cos\beta) \begin{cases} \cos m\gamma & m \geq 0 \\ \sin |m|\gamma & m < 0 \end{cases} \tag{6}$$

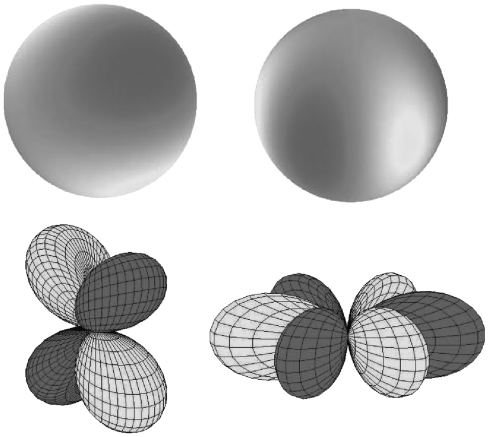

a) b)

Fig. 4 Spherical harmonic weighting functions: a) zonal, $Y_{2,-1}$; and b) sectoral, $Y_{3,-3}$.

where $\Phi_l^m(\cos\beta)$ is the associated Legendre function $\{l, m\} \in \mathbb{Z}$, $l \geq 0$, $|m| \leq l$, and the factor N_l^m is a normalization coefficient. The resulting wide-field integrated outputs for component weighting functions $\mathbf{F}_{l,m}^k = Y_{l,m}^k \hat{\mathbf{e}}_k$ for $k \in \{\gamma, \beta\}$ are then given by

$$y_{l,m}^k(\mathbf{x}) = \langle \dot{\mathbf{Q}}, \mathbf{F}_{l,m}^k \rangle = \int_0^{2\pi} \int_0^{\pi} \dot{Q}_k(\mathbf{x}) Y_{l,m}^k \sin\beta \, \mathrm{d}\beta \, \mathrm{d}\gamma \tag{7}$$

D. Interpreting Wide-Field Integration Outputs

The objective is to characterize the relationship between the component weighting functions $\mathbf{F}_{l,m}^k = Y_{l,m}^k \hat{\mathbf{e}}_k$ and the relative state:

$$\mathbf{x} = \{y, z, \phi, \theta, \psi, u, v, w, p, q, r\} \mathbb{R}^n$$

encoded by the projections in Eq. (7). This is achieved by linearizing the $y_{l,m}^k$ about a nominal optic flow pattern. A desired (equilibrium) optic flow pattern is specified by a predefined amount of longitudinal and lateral asymmetry (Fig. 3). Physically, this is attained when the vehicle is centered between arbitrarily spaced obstacles and is flying straight and level at some desired altitude above ground. This is expressed mathematically by the nominal trajectory:

$$\mathbf{x}_0 = \{0, 0, 0, 0, 0, u_{\text{ref}}, 0, 0, 0, 0, 0\}$$

where u_{ref} is the target forward speed.

To provide an intuitive illustration of the linkages between outputs and weighting patterns, consider a tunnel environment with infinitely high walls, $(b_N, b_S, h_U, h_D) \to \infty$ and $a_E = a_W$. Several harmonic decompositions using this optic flow model are presented in Fig. 5. For example, $y_{0,0}^\beta$ provides a measure of the heave velocity when the signal is linearized about $\mathbf{x}_0$. It quantifies the goodness of the match between the actual optic flow pattern and a purely longitudinal template pattern defined by the harmonic $Y_{0,0}^\beta$, which has constant magnitude for all points on the sphere. A climbing vehicle experiences longitudinal optic flow on both sides of the vehicle, and this deviation from the nominal pattern is captured by the WFI output $y_{0,0}^\beta$. The $Y_{1,1}^\beta$ harmonic weights the front and rear of the vehicle strongly but with opposite signs, thus capturing any forward–aft optic flow asymmetry (induced by pitch axis rotation) in the decomposition. The lateral offset from the tunnel center is captured by the $y_{2,2}^\gamma$ output, which places large negative azimuthal flow weights on both sides of the vehicle. If the vehicle is nearer the right-side wall, the optic flow will be larger on that side (where azimuthal flow is positive), thus the WFI output will be negative. If the left-side wall is nearer, then the negative-direction azimuthal optic flow will be stronger, and the output will be positive. The positive weighting of the optic flow at the front and rear of the vehicle acts to filter out yaw rotation motion from the decomposition.

III. Optimal Static Estimation of Relative States

Optic flow cannot be measured directly; it must be inferred from the spatiotemporal patterns of the luminance incident on an imaging

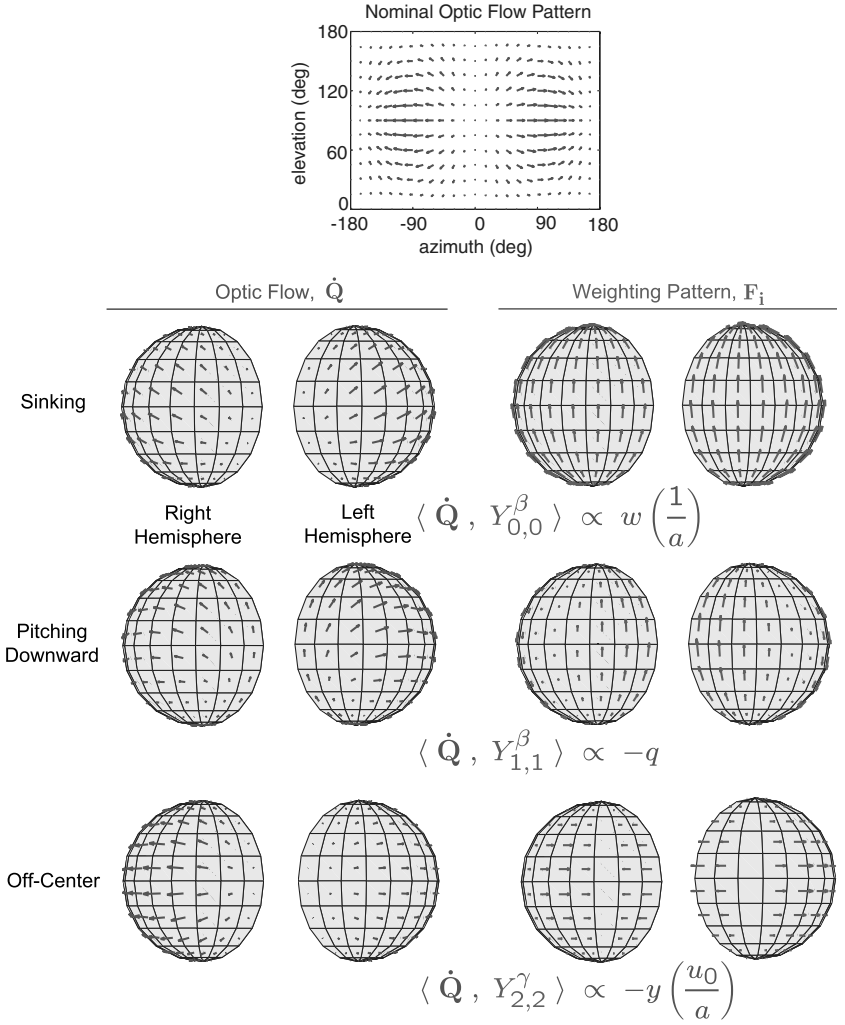

Fig. 5 Decomposing optic flow using spherical harmonics: WFI outputs indicate perturbations to the nominal optic flow pattern (top of figure) and are scaled functions of state.

surface. Therefore, the optic flow estimation process introduces error in the measurements, which is compounded by sensor noise and contrast/texture variations occurring in the environment. Additional uncertainty associated with the nearness function is present due to the variation in the obstacle distributions from the baseline environments, assumed in Sec. II.B. In this section, an offline procedure for determination of optimal weighting patterns for static estimation of relative states that accounts for these uncertainties in the optic flow model in Eq. (3) and the environment in Eq. (4) is developed.

A. Measurement Model

Given $M \geq n$ linearly independent weighting functions $\mathbf{F}_{\mathbf{y}} = \{\mathbf{F}_{y_j},\ j = 1,\ \ldots,\ M\}$, the WFI outputs in Eq. (7), using the optic flow model in Eq. (3), can be linearized for small perturbations about $\mathbf{x}_0$, which will yield linear output equations of the form $\mathbf{y} = C\mathbf{x}$. Accounting for environment uncertainty and measurement noise, the observation equation becomes

$$\tilde{\mathbf{y}} = C\mathbf{x} + \mathbf{w}; \qquad C = C_0 + \delta C \tag{8}$$

where $\tilde{\mathbf{y}} \in \mathbb{R}^M$ are the measured outputs, the noise $\mathbf{w}$ is zero mean $E\{\mathbf{w}\} = 0$ with covariance $E\{\mathbf{w}\mathbf{w}^T\} = R_{\mathbf{w}}$. The quantity δC is assumed to be a zero mean random perturbation $E\{\delta C\} = 0$, which captures the variation in the nearness function $\mu(\gamma,\ \beta,\ \mathbf{q})$ from the mean C_0. It is further assumed that $E\{\mathbf{w}\delta C^T\} = 0$. Without a priori knowledge of the statistical distribution of environments that the vehicle will encounter, C_0 is approximated with an unweighted average of the four cases described in Sec. II.B:

$$C_0 = \tfrac{1}{4}[C(a_E = \infty,\ a_W = \infty) + C(a_E = 1,\ a_W = \infty) + C(a_E = \infty,\ a_W = 1) + C(a_E = 1,\ a_W = 1)] \tag{9}$$

where $a_{E,W} = 1$ m defines a practical minimum for the nominal wall clearance or the half-width of any tunnels an MAV might encounter.

B. Weighted Least-Squares Inversions

The problem is now posed in the form of a standard static linear estimation problem, in which one seeks the solution of an overdetermined, inconsistent set of linear equations, given by Eq. (8). The optimal choice that minimizes the weighted ($W > 0$) sum square of the residual errors $J = \frac{1}{2}(\tilde{\mathbf{y}} - C\hat{\mathbf{x}})^T W(\tilde{\mathbf{y}} - C\hat{\mathbf{x}})$ is given by $\hat{\mathbf{x}} = C^{\dagger}\tilde{\mathbf{y}}$, where

$$C^{\dagger} = (C_0^T W C_0)^{-1} C_0^T W \tag{10}$$

The choice for the weighting matrix that acts to penalize high measurement noise and/or environmental model uncertainty is $W = (R_{\mathbf{w}} + R_{\delta C})^{-1}$. To obtain an expression for $R_{\mathbf{w}}$, it is first assumed that optic flow measurements taken at discrete locations on the sphere are affected by 2-D zero mean additive noise $\boldsymbol{\eta}(\gamma,\ \beta)$ with variance σ_{η}^2, with no correlation between dimensions, measurement nodes, or with signal magnitude. Under these assumptions, the measurement noise at the level of the integrated output is $w_i = \langle \boldsymbol{\eta},\ \mathbf{F}_{y_i} \rangle$, and the noise covariance is given by $E\{\mathbf{w}\mathbf{w}^T\}$. Using linearity of Eq. (7) and the properties of the covariance matrix, one obtains:

$$R_{\mathbf{w},ij} = \Delta\beta\Delta\gamma\sigma_{\eta}^2 \langle \mathbf{F}_{y_i},\ \mathbf{F}_{y_j} \rangle \tag{11}$$

where $\Delta\beta$ and $\Delta\gamma$ are set to 9 deg. Note that the measurement noise at the level of the WFI outputs approaches zero as the number of measurement nodes on the imager approaches infinity, providing significant improvement in the signal-to-noise ratio: an attractive property of the WFI processing approach.

To obtain an expression for $R_{\delta C}$, it is assumed that no prior knowledge of $\mathbf{x}$ is available and that $R_{\delta C}$ should consider all states equally without cross-state weightings. It follows that the elements of the model uncertainty penalty matrix can be computed as

$$R_{\delta C,ij} = \varepsilon \sum_{k=1}^{n} \text{cov}\,(\delta C_{ik},\ \delta C_{jk}) \tag{12}$$

where ε is a weighting constant that can be adjusted to specify the relative importance between the measurement noise $\mathbf{w}$ and the model uncertainty δC in the estimator. To compute $R_{\delta C}$ based on the assumed model in Eq. (4), the covariance terms are conservatively approximated using just the four extreme δC matrices. In the limit, as $\varepsilon \to 0$, one recovers the well-known minimum variance Gauss–Markov estimator, but the state estimates will be less robust to environment uncertainties. Setting $\varepsilon \gg \sigma_\eta^2$ tends to result in estimates that are not robust to noise. Iteration with the simulation (Sec. V) resulted in selection of $\varepsilon = \sigma_\eta^2$. The absolute magnitude of these terms does not affect the estimator; only relative magnitude is important.

C. State Extraction Weighting Functions

Optimality of the inversion in Eq. (10) is with respect to the span of the basis function set, which defines the search space. In practice, inclusion of spherical harmonics up to the 10th degree, constituting $M = 242$ independent weighting functions, provides a sufficient span to achieve reasonable convergence to the global $L^2(S^2, \mathbb{R}^2)$ optimum. Instead of computing M inner products in real time, computational requirements can be streamlined by leveraging the linearity of the WFI operator. Consider relative state estimates $\hat{\mathbf{x}} = C^\dagger \tilde{\mathbf{y}}$, where $\tilde{\mathbf{y}} = \langle \dot{\mathbf{Q}},\ \mathbf{F}_\mathbf{y} \rangle$. If the inversion is pushed through the inner product, one obtains:

$$\hat{x}_i = \left\langle \dot{\mathbf{Q}}, \sum_{j=1}^{M} C_{ij}^\dagger \mathbf{F}_{y_j} \right\rangle \tag{13}$$

for which the second argument in the inner product can be interpreted as the optimal extraction pattern for the ith state:

$$\mathbf{F}_{\hat{x}_i} = \sum_{j=1}^{M} C_{ij}^\dagger \mathbf{F}_{y_j}$$

These patterns are presented in Fig. 6.

When a relative state becomes nonzero, it imposes a perturbation pattern upon the nominal optic flow pattern. These patterns are not necessarily orthogonal to other state-induced patterns, thus the optimal inversion generates weighting functions $\mathbf{F}_{\hat{\mathbf{x}}}$ that act to remove the coupling due to nonorthogonal states. It also concentrates weightings on areas of the environment that are more consistent across the modeled family. For example, the forward speed extraction pattern (Fig. 6) weights terrain-driven optic flow rather than that arising from lateral obstacles. The noise penalty term in W acts as a counter balance to this, ensuring that a spatially broad weighting field is preserved in order to retain the noise mitigation benefits of averaging. Without this, the patterns would be highly localized.

D. Partial Field of View

It has been assumed that the vehicle can measure optic flow over the entire spherical viewing arena, but this may create hardware design complications and possible optic flow computation issues if the sky is uniformly blue or overcast. A rotating vehicle will not induce a rotation field on a zero-contrast background, thus all WFI-based relative states will be distorted, leading to potential instability. It is therefore beneficial for robustness to measure optic flow below the horizon only, where the existence of suitable image contrast is more probable. The measurement domain can theoretically be arbitrarily small and still permit relative state estimates via WFI; however, the estimates will become less robust to noise as the field of view decreases.

The Cramer–Rao bound states that any inversion of the observation equation will result in a state estimate covariance matrix $P = E\{(\hat{\mathbf{x}} - \mathbf{x})(\hat{\mathbf{x}} - \mathbf{x})^T\}$ that is bounded below by the inverse of the Fisher information matrix $P \geq (C^T R_\mathbf{w}^{-1} C)^{-1}$. It is realized with equality under Eq. (10), if $\delta C = 0$. For a partial field of view, the norm of $(C^T R_\mathbf{w}^{-1} C)^{-1}$ provides a means of evaluating the relative noise throughput (mapping from $\|\boldsymbol{\eta}\|$ to $\|\mathbf{w}\|$). Using Eqs. (9) and (11), it is found that this norm roughly triples by restricting the field of view to below the horizon only. This is deemed an acceptable price for the ability to operate in conditions in which the sky has no visual contrast. The optimum weighting patterns were obtained with a lower hemisphere measurement grid, but these plots have been omitted for brevity. The default design still uses the full spherical measurement grid, but a performance comparison has been made with the alternative half-sphere configuration (Figs. 9c and 9d).

IV. Feedback Control Design

In this section, it is shown how the relative state estimates $\hat{\mathbf{x}}$ can be used to stabilize an MAV about a desired relative state $\mathbf{x}_\text{ref}$ with conventional linear state feedback techniques $\mathbf{u} = -K(\hat{\mathbf{x}} - \mathbf{x}_\text{ref})$. Static, rather than dynamic, compensation is employed to be consistent with a low-computation paradigm. The vehicle selected for simulation is the 390 g E-Sky hobby helicopter, with a 50.5 cm main rotor diameter and a 14.5 cm tail rotor. A linearized flight dynamics model was obtained in a prior study [44] via system identification with the U.S. Army's CIFER software package. The kinematics and dynamics are linearized about the forward flight condition, with $u_\text{ref} = 1$ m/s (Appendix A). For simulation, the full nonlinear kinematic equations are used.

The feedback control objective is to regulate the relative state estimates provided by WFI to specified reference values, thereby generating stable obstacle avoidance and terrain-following behaviors. The proposed methodology assumes that an altitude measurement $\tilde{z}$ is available for feedback, along with the actuator states $(\xi, \chi, \Omega_\text{mr})$. The independent altitude measurement is required to remove target altitude dependence on obstacle distribution in the environment (Sec. VI). The estimates for the remaining 10 relative states are generated using the optimal weighting functions $\mathbf{F}_{\hat{\mathbf{x}}} = C^\dagger \mathbf{F}_\mathbf{y}$:

$$\hat{x}_i = \langle \dot{\mathbf{Q}},\ \mathbf{F}_{\hat{x}_i} \rangle + C_{i,M+1}^\dagger \tilde{z} \tag{14}$$

where $\mathbf{F}_\mathbf{y}$ is an $(M+1) \times 2$ matrix of the spherical harmonic patterns, and the $M+1$ is a column of $C^\dagger$, corresponding to the independent attitude measurement $\tilde{z}$.

The desired reference for the state vector

$$\mathbf{x} = (y,\ z,\ \phi,\ \theta,\ \psi,\ u,\ v,\ w,\ p,\ q,\ r,\ \xi,\ \chi,\ \Omega_\text{mr})$$

which accounts for the pitch and rotor speed variation from hover required to reach 1 m/s, is taken as

$$\mathbf{x}_\text{ref} = (0,\ -K_{z,\theta}(\hat{\theta} - \tilde{\theta}),\ 0,\ -0.05,\ 0,\ 1.00,\ 0,\ -0.05,\ 0,\ 0,\ 0,\ 0,\ 0,\ 0.21) \tag{15}$$

Note the target altitude offset $z_\text{ref} = -K_{z,\theta}(\hat{\theta} - \tilde{\theta})$ is a function of the pitch angle measurement relative to the gravity vector $\tilde{\theta}$ (assumed to be provided by an additional sensor) and the WFI estimate $\hat{\theta}$ from Eq. (14), which provides an indication of upcoming terrain. This form of the reference is chosen in order to avoid unacceptable speed loss during climbs over steep terrain. To prevent excessive or unnecessary vertical velocities, z_ref is intentionally restricted to be zero, except when in the range $(-1, 0)$. Furthermore, the pitch angle estimate $\tilde{\theta}$ is subtracted from the WFI-based estimate $\hat{\theta}$ to preclude

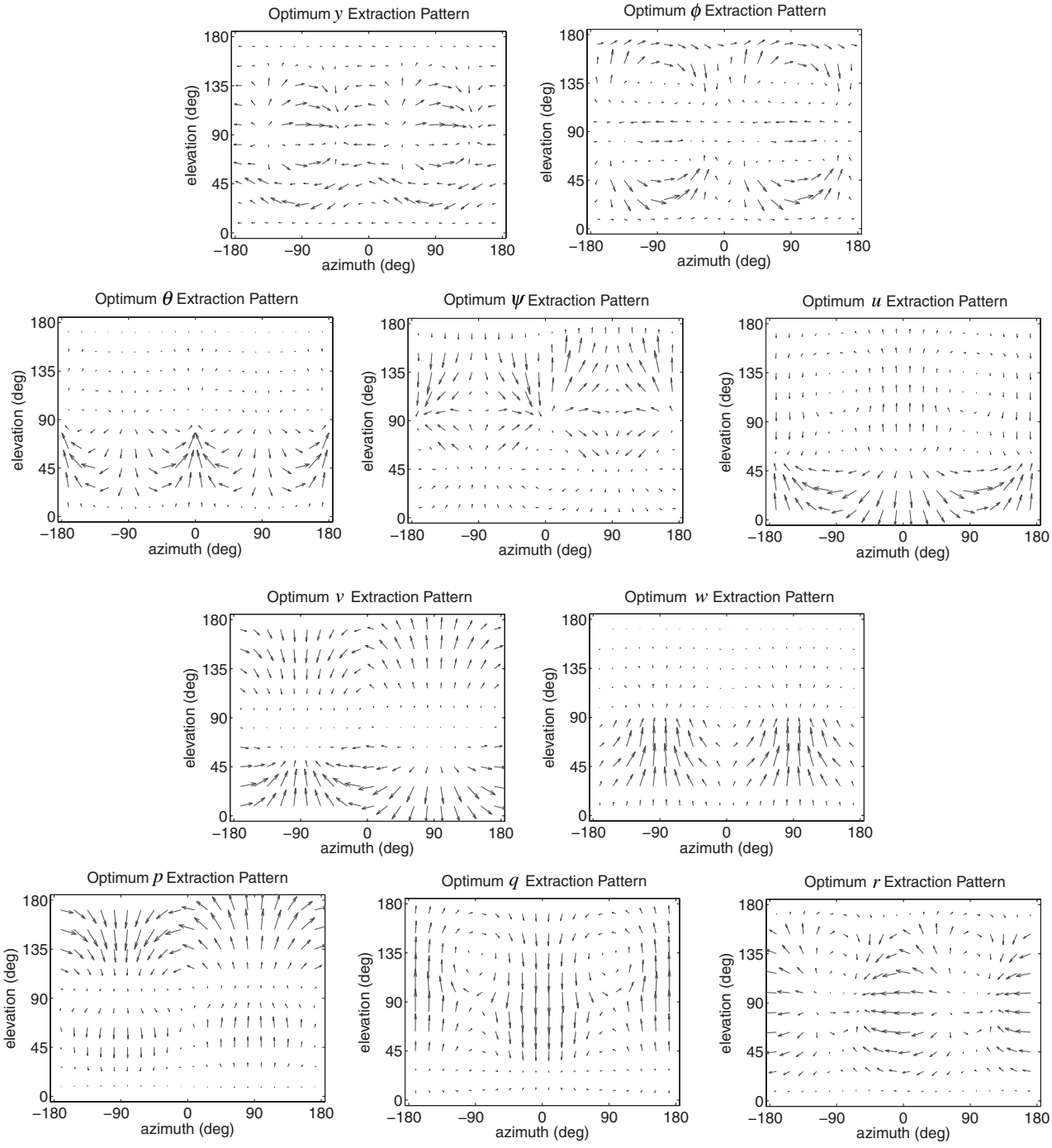

Fig. 6 Optimum weighting patterns to recover environment-scaled states from the optic flow pattern.

superfluous climb commands arising from the nominal specified value of $\hat{\theta} = -0.05$.

The structure of the final feedback control law is

$$u_k = -\sum_i K_{k,x_i}(\langle \dot{\mathbf{Q}}, \mathbf{F}_{\hat{x}_i} \rangle + C^{\dagger}_{i,M+1}\tilde{z} - x_{i,\text{ref}}) - \sum_j K_{k,x_j}(\hat{x}_j - x_{j,\text{ref}}) \tag{16}$$

where $k = \{\Lambda_{\text{lat}}, \Lambda_{\text{lon}}, \Lambda_{\text{t}}, \Lambda_{\text{yaw}}\}$ denotes the actuator input, $i = \{y, \phi, \psi, u, v, w, p, q, r\}$ is the set of WFI-based state measurements, and $j = \{z, \theta, \xi, \chi, \Omega_{\text{mr}}\}$ is the set of states measured with or estimated from alternate sensors. Infinite horizon linear quadratic regulation (LQR) [45] is employed to obtain a set of optimal feedback gains. After iteration with the simulator (described in Sec. V), the LQR state penalty matrix was set to

$$J_{\mathbf{x}} = \text{diag}(25, 1, 1, 1, 5, 100, 20, 5, 1, 1, 1, 10^{-15}, 10^{-15}, 10^{-15})$$

and the control penalty matrix was set to $J_{\mathbf{u}} = \text{diag}(1, 1, 1, 1)$. Table A2 lists the final gains, and Sec. VI examines the stability of the vehicle across the range of modeled environments.

V. Simulation

In this section, the methodology and results are presented for simulation of a helicopter in a scenario that can be likened to a reconnaissance vehicle flying through an urban environment. The weighted integrals of the measured optic flow signals provide adequate information to stabilize and navigate with the linearized vehicle model (see Sec. VI). There are no guarantees, however, in the presence of measurement noise, nonlinearities, and differences between the true environment and its mathematical approximation.

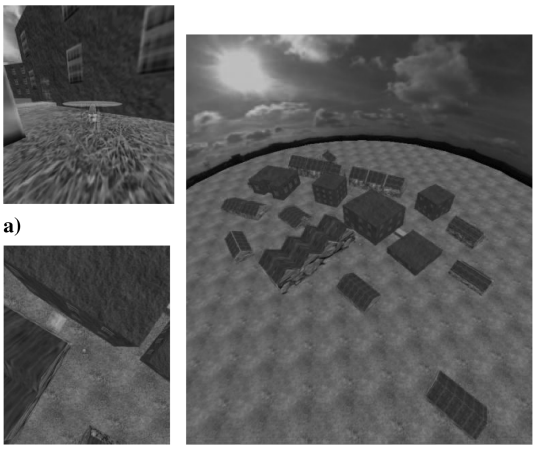

a) b) c)

Fig. 7 3-D simulation environment.

Here, it is demonstrated in simulation that the vehicle can successfully perform the goal of obstacle avoidance and terrain following in the presence of noise and model environment uncertainty.

A. Methodology

Our in-house simulation environment provides visualization capabilities as well as the ability to compute optic flow from simulated cameras. The virtual MAV is installed with six cameras, each with a 90×90 deg field of view and a resolution of 128×128 pixels. The cameras cover the six sides of a cube, such that the full spherical viewing arena is imaged.

The imagery is first passed through a Gaussian blurring function to mitigate aliasing issues. Optic flow is computed with a resolution iterative implementation of the Lucas–Kanade algorithm at 60 fps for 800 image points. The points are distributed in a uv-coordinate spherical grid, with constant angular spacing between nodes, and are mapped from a virtual sphere surface to the flat cameras via geometric projection. The environment surfaces and sky are textured with imagery of sufficient visual contrast, so that optic flow can be computed. The optic flow measurements are desampled from 800 to 200 by unweighted averaging of square groups of four adjacent nodes. Outlier measurements with a high final cost function or infeasibly large shift estimates are ignored in the block average. This step reduces noise, because some areas of the viewing arena may still have poor contrast. The simulation process is illustrated in Fig. 8.

To demonstrate robustness with respect to initial conditions, a Monte Carlo approach was employed. Twenty initial headings and (x, y) locations were generated using a uniform distribution, excluding parts of the environment covered by buildings.

B. Results

Figure 9 shows that, from all initial conditions, the helicopter is able to successfully avoid the obstacles while maintaining a target height of 1 m above the ground. This is achieved almost entirely with optic-flow-based measurements, with the exception of the independent pitch angle, altitude, and actuator-related state measurements.

There are several instances in which the helicopter heads back toward the buildings after clearing the obstacle course, but this is a reaction to the large sky dome that surrounds the environment (Fig. 7c). Figure 9e shows the helicopter climbing over a box completely obstructing its path, which is made possible by the adjustment of target altitude. The terrain pitch angle spikes as the helicopter approaches the box, which pushes the target altitude up, forcing the vehicle to temporarily track an altitude above ground greater than 1 m in order to more safely approach the upcoming terrain. Restricting the measurement grid to the lower hemisphere (Figs. 9c and 9d) resulted in a roughly similar performance but eventual deviation in the trajectories due to differences in the y and ψ estimates. The full measurement grid covers the entire height of the buildings, thus the vehicle has stronger and earlier warnings of lateral obstacles. The lower hemisphere grid covers only the lower section of the buildings, thus delaying the spiking of the WFI-based obstacle indicators.

Figures 10 and 11 show the states and measurements for part of the Fig. 9c trajectory (during the second major turn). The asymmetry in the optic flow pattern that prompts an avoidance maneuver is evident from Fig. 11. In the z plot, the true curve describes the vertical trajectory with respect to the inertial frame, but the measured $\tilde{z}$ shows the deviation from the desired height above ground (which is regulated to a target level accounting for the upcoming terrain). For both the z and θ plots, this difference in reference frames explains apparent discrepancies. Despite the fact that the WFI delivers environment-sensitive state estimates, the measurements still satisfactorily track the true quantities. The low noise levels are attributable to the white-noise mitigation property of the WFI and the outlier rejection step in the spatial filtering of the optic flow measurements. The environment-related scaling error in the ϕ estimate does not compromise roll stability, but the high gain on the ψ and y does lead to oscillations from the feedback of finite noise.

VI. Discussion

Optic flow is a relative measure, thus the state estimates obtained in this study are generally scaled combinations of speed/depth. In this paper, it has been shown that these quantities are sufficient for regulating a safe optic flow pattern, and hence a safe trajectory. One complication of this is that pure WFI-based control will cause the

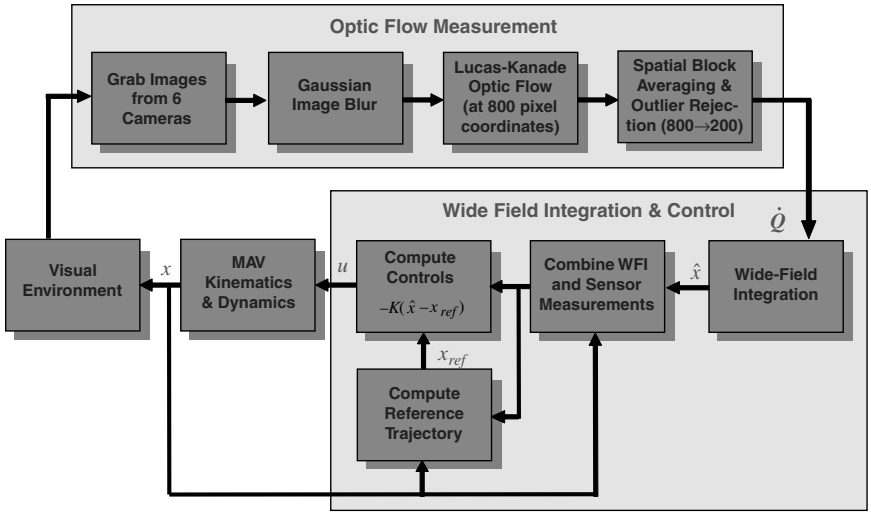

Fig. 8 Simulation process diagram.

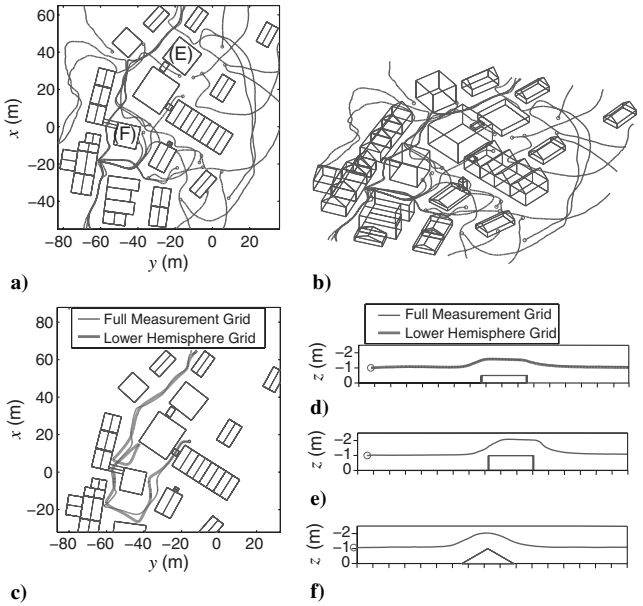

Fig. 9 Simulation results of trajectories: a) and b) trajectories using full measurement grid; c) comparison of full- and half-sphere measurement grid; d) side view comparison during navigation over 0.5 m box; e) 1 m box; and f) 1 m ramp.

vehicle to regulate a lower altitude when obstacles are tightly spaced. From a safety viewpoint, this is undesirable, which is why an independent measurement of $\tilde{z}$ was assumed available in this study. In contrast, it may be beneficial to link forward speed with lateral obstacle spacing using a weighting pattern, such as that shown in Fig. 3a, to measure u. This strategy is beyond the scope of the study.

Although the simulations demonstrate apparent stability, it is of interest to examine theoretical stability and the potential for this concept to be applied in other scenarios. LQR guarantees a stable small perturbation system, given a perfect vehicle model ($\dot{\mathbf{x}} = A\mathbf{x} + B\mathbf{u}$) and a perfect state knowledge. Stability in the presence of aerodynamic model perturbations could be evaluated with a structured singular value analysis, but the focus of this paper is WFI processing, thus no such analysis is included. The latter assumption will, in general, be violated due to environment dependency in the state estimates. It is therefore pertinent to check that this does not compromise the stability.

The observation equation describing the linearized information contained in the state estimates is

$$\hat{\mathbf{x}} = C_{\hat{\mathbf{x}}}\mathbf{x} = (\text{diag}\{1,\ 0,\ 1,\ 0,\ 1,\ 1,\ 1,\ 1,\ 1,\ 1,\ 1,\ 0,\ 0,\ 0\}C^{\dagger}C + \text{diag}\{0,\ 1,\ 0,\ 1,\ 0,\ 0,\ 0,\ 0,\ 0,\ 0,\ 0,\ 1,\ 1,\ 1\})\mathbf{x} \qquad (17)$$

where $C_{\hat{\mathbf{x}}} \neq I$ if $C \neq C_0$. The linear stability analysis proceeds by ensuring that the eigenvalues of $A_{\text{cl}} = (A - BKC_{\hat{\mathbf{x}}})$, the inner loop, lie in the open left half of the plane. Because the state-dependent reference condition accounts for the unmodeled (nonflat) terrain, it does not affect the small perturbation stability within the context of our modeled flat environment. From the numerical eigenvalue analysis (see Fig. 12), it is found that the linearized system is indeed closed-loop stable across the entire family of modeled outdoor environments.

The eigenvalue method can also be used to evaluate stability in other environments. In the large perturbation regime, stability could be demonstrated by nonlinear methods similar to the Lyapunov analysis performed for a planar vehicle in [35]. The simulation results presented here demonstrate applicability beyond the simple environment model. With the WFI methodology, the vehicle attempts to track an obstacle-symmetric path through its world (essentially approximating the optic flow pattern as an infinite tunnel), a characteristic that is independent of environment structure. Different behaviors can be rapidly realized during flight by adjusting the target state in Eq. (15), which specifies desired optic flow asymmetry. Setting a nonzero y_{ref}, for example, will cause the vehicle to track a noncentered path or (in the extreme) hug a wall.

Note that the possibility of a collision course into a symmetric obstacle is finite but small because such trajectories are unstable [35]. There are several close encounters in Fig. 9, but when the helicopter becomes near enough, small asymmetries become stronger, enabling an avoidance maneuver before impact. Despite exclusion of a front-side wall from the environment model, the designed weighting patterns are still useful in these near-head-on approaches. However, the instances during symmetric approaches to building walls or corners (which generate minimal optic flow), where proximity becomes unsafe, suggest the need for an emergency turn or continuous control capability based on feedback of a WFI-based $\mathbf{x}$ (frontal proximity) estimate [14,46]. This estimate pattern could be obtained using the inversion of WFI outputs within the enclosed room environment in Eq. (4). The inherent limitation is that small obstacles generate high frequency perturbations to the optic flow signal that are filtered out by WFI. For avoidance of such obstacles (i.e., poles and wires), one could implement detection of these high frequency anomalies or make use of a forward-pointing range finding sensor, such as sonar [47]. The WFI technique presented in this paper is suited to the avoidance of large obstacles.

With regard to concept feasibility, existing MAVs are capable of obtaining attitude and angular rate estimates through the use of gyros, accelerometers, and magnetometers [48]. A pitch attitude sensor is therefore easily attainable, and lightweight sonar sensors are available for measurement of height [48,49]. Rather than relying on optic flow for the remaining nine states, an improved configuration might employ an onboard inertial measurement unit to provide attitude and rate measurements (due to its superior accuracy). The niche for optic-flow-based sensing on MAVs is not an accurate state

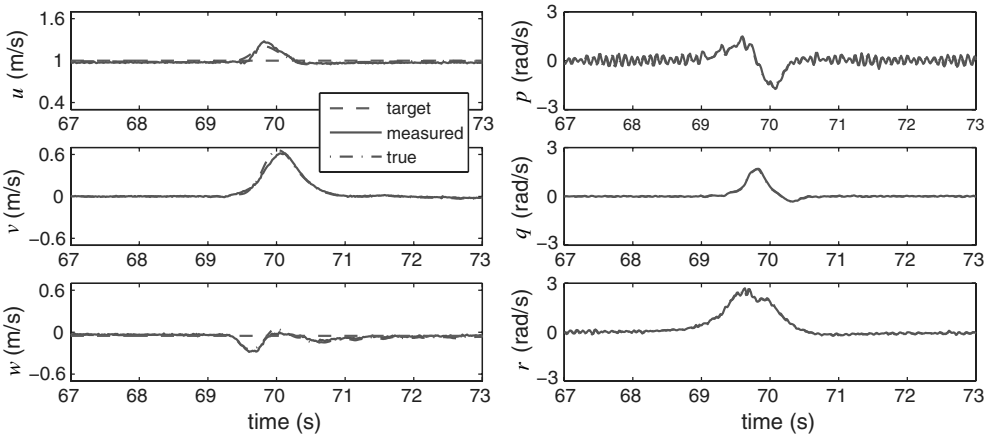

Fig. 10 Speeds, rates, and optic-flow-extracted measurements are plotted for simulation results for the full spherical measurement grid case shown in Fig. 9c during a 90 deg turn.

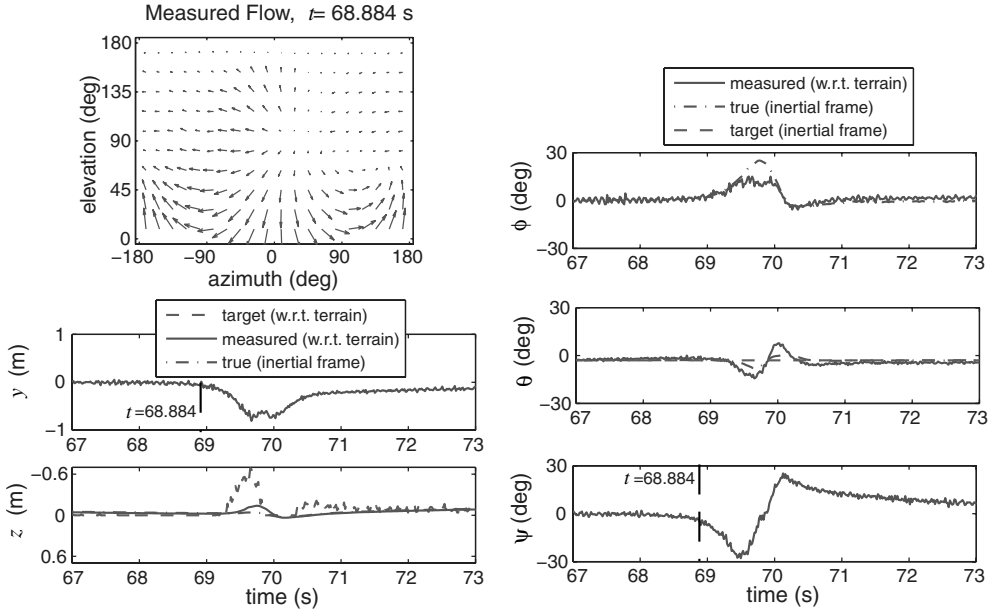

Fig. 11 Vehicle pose, WFI outputs, and measured optic flow are plotted for simulation results for the full spherical measurement grid case shown in Fig. 9c during a 90 deg turn (w.r.t. denotes with respect to).

estimation but a relative proximity and velocity estimation. With respect to camera configuration, the setup proposed in this paper is academic, but a similar feasible realization is certainly possible. Because lower hemisphere measurements are sufficient, one could use a single camera and a panoramic mirror [50]. Corridor-following WFI demonstrations have been made with such a setup on a wheeled ground robot [35,51] and a micro helicopter [49].

To compare results with similar studies, the ability to successfully navigate a cluttered field makes this study comparable with [17]. A previous WFI study, with a fixed-wing vehicle [52], achieved a similar feat, but measurements were confined to three orthogonal rings of optic flow rather than the full sphere. Consequently, objects not appearing in the pitch plane or yaw plane would not be avoided. The centering behavior demonstrated in Fig. 9 outperforms the optic-flow-controlled trajectories in [15], because only the lateral offset is controlled in that study instead of offset and orientation. Similarly, the terrain-following performance improves on [21,22] for the same reason, but in the vertical plane. An algorithm developed in [20] potentially offers a more robust obstacle avoidance by detecting impingements on a spherical tunnel, but it assumes independent knowledge of vehicle motion.

In terms of motion estimation and terrain mapping, WFI does not provide explicit information about environment structure, as in [23,27], but it does enable motion-state extraction with noise levels and accuracies, similar to those reported in [27,30] and superior to those reported in [23]. Even lower noise is achieved in [24], but high contrast feature tracking is employed, which is computationally expensive. Although optic flow computations in our study make use of a digital processor and modern optic flow algorithm, the attractive potential of WFI is its low computational burden and suitability for analog implementation [40]. The disadvantage is that this implementation does not perform well in environments with large areas of poor contrast, a limitation of the dynamic range of modern imaging devices. This could potentially be overcome through use of adaptive analog imaging and/or different optic flow algorithms (i.e., block matching). For this reason, most vision-based navigation studies use feature detection/tracking [53], but the associated computational requirements are generally too large for implementation on MAV avionic hardware (i.e., small fixed point processor) at high bandwidth.

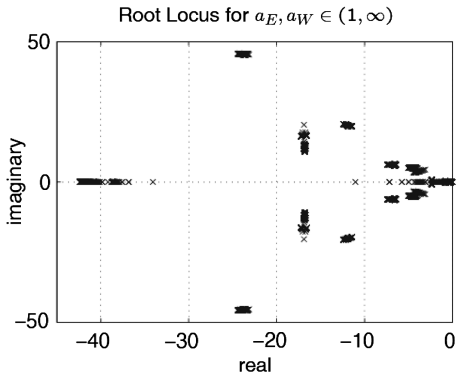

Fig. 12 Root locus diagram for range of wall spacings. Closed-loop eigenvalues computed for a_W and a_E, independently ranging from 1 to 1000 m ($\sim\infty$) in steps of 1 m.

VII. Conclusions

This paper demonstrates that optic-flow-based WFI techniques can be extended to 6-DOF vehicles. Measurements of the spherical 2-D optic flow pattern, integrated against various weighting patterns, provide MAVs with information reliable enough to stabilize the vehicle and navigate an unknown environment. Using algebraic approximation of simple 3-D worlds, one can predict relative state information that can be decoded from optic flow measurements using spatial decompositions of the optic flow pattern. Weighting patterns were derived using an optimal inversion technique that provided the best scaled estimates of relative states, given noisy measurements and uncertainty in the environment. For the linearized model of a micro helicopter, LQR inner loop control was augmented with a variable target altitude to enhance its ability to climb steep terrain. The eigenvalues of the static output–feedback system were shown to be stable across the entire family of modeled environments, and when simulated in a cluttered field, the helicopter successfully avoided obstacles and terrain anomalies. Real-time implementation requires just 10 weighted summations of 200 optic flow measurements per control update. Given the current lack of sensors with suitable mass and bandwidth for MAVs, WFI implementations could provide an attractive alternative for stability augmentation and collision avoidance in the field.

Appendix A: Micro Air Vehicle Dynamics and Control

The dynamics equations of motion are given in Eq. (A1). The actuator saturation limits are $|\Lambda_{\text{lat}}| \leq 1$, $|\Lambda_{\text{lon}}| \leq 1$, $|\Lambda_t| \leq 0.5$, and $|\Lambda_{\text{yaw}}| \leq 1$. Characteristic stability quantities are defined in Table A1 with SI units, and all symbols have their usual flight dynamics

interpretations. The kinematics equations were linearized about $\mathbf{x}_0$ for the LQR computation, and the LQR results are in the first four columns of Table A2.

$$\begin{aligned}
\dot{u} &= -g\theta + X_u u; \qquad \dot{v} = g\phi + Y_v v - u_{\text{ref}} r \\
\dot{w} &= Z_w w + Z_{\Omega_{\text{mr}}}\Omega_{\text{mr}} + u_{\text{ref}} q; \qquad \dot{p} = L_v v + L_\xi \xi \\
\dot{q} &= M_u u + M_\chi \chi; \qquad \dot{r} = N_r r + N_{\Lambda_{\text{yaw}}}\Lambda_{\text{yaw}} \\
\dot{\xi} &= -p - \frac{1}{\tau_f}\xi + \frac{\xi_\chi}{\tau_f}\chi + \frac{\xi_{\text{lat}}}{\tau_f}\Lambda_{\text{lat}} + \frac{\xi_{\text{lon}}}{\tau_f}\Lambda_{\text{lon}} \\
\dot{\chi} &= -q + \frac{\chi_\xi}{\tau_f}\xi - \frac{1}{\tau_f}\chi + \frac{\chi_{\text{lat}}}{\tau_f}\Lambda_{\text{lat}} + \frac{\chi_{\text{lon}}}{\tau_f}\Lambda_{\text{lon}} \\
\dot{\Omega}_{\text{mr}} &= T_{\Omega_{\text{mr}}}\Omega_{\text{mr}} + T_{\Lambda_t}\Lambda_t
\end{aligned} \tag{A1}$$

Appendix B: Nearness Function Derivation

Consider the general scenario of a vehicle surrounded by flat surfaces positioned north, east, south, west, up, and down, relative to the inertial vehicle frame. The desired position of the vehicle is some nominal location within the enclosed room. When the vehicle deviates from its nominal position (Fig. 2a), the deviation is captured by the orthogonal quantities (x, y, z). The objective is to find a model for the distance to obstacles in this general environment.

Expressed as a vector quantity, the distance to a surface along the direction $\hat{\mathbf{e}}_r$ from a point $\mathbf{r}$ on the sphere is $\mathbf{d} = d(\gamma, \beta, \mathbf{q})\hat{\mathbf{e}}_r$, assuming that $\|r\| \ll \|d(\gamma, \beta)\|$. For the surface below the vehicle (Fig. 2b), the altitude is denoted as $h_D - z$. The component of $\mathbf{d}$ along the direction of the fixed frame $\mathcal{F}$ vertical $\hat{\mathbf{e}}_z$ is therefore given by

$$\langle \mathbf{d}, \hat{\mathbf{e}}_z \rangle = h_D - z \tag{B1}$$

To derive the general expression for $\mu(\gamma, \beta, \mathbf{q}) = 1/d(\gamma, \beta, \mathbf{q})$, the vector $\mathbf{d}$ needs to be expressed in $\mathcal{F}$ coordinates for a general orientation to facilitate the extraction of the $\hat{\mathbf{e}}_z$ component. Consider the spherical coordinate unit vector $\hat{\mathbf{e}}_r$ (Fig. 1) expressed in $\mathcal{B}$ frame coordinates:

$$[\hat{\mathbf{e}}_r]_{\mathcal{B}} = \begin{pmatrix} \sin\beta\cos\gamma \\ \sin\beta\sin\gamma \\ \cos\beta \end{pmatrix} \tag{B2}$$

For an arbitrary orientation of the body frame $\mathcal{B}$, parameterized by 3-2-1 Euler angles (ψ, θ, ϕ), the components of $\hat{\mathbf{e}}_r$ expressed in $\mathcal{F}$ coordinates are given by $[\hat{\mathbf{e}}_r]_{\mathcal{F}} = \mathcal{R}_{\mathcal{BF}}^{-1}[\hat{\mathbf{e}}_r]_{\mathcal{B}}$:

$$[\hat{\mathbf{e}}_r]_{\mathcal{F}} = \begin{pmatrix} c\theta c\psi & c\theta s\psi & -s\theta \\ s\phi s\theta c\psi - c\phi s\psi & s\phi s\theta s\psi + c\phi c\psi & s\phi c\theta \\ c\phi s\theta c\psi + s\phi s\psi & c\phi s\theta s\psi - s\phi c\psi & c\phi c\theta \end{pmatrix}^{-1} \begin{pmatrix} s\beta c\gamma \\ s\beta s\gamma \\ c\beta \end{pmatrix} \tag{B3}$$

Hence, the $\hat{\mathbf{e}}_z$ component of $\mathbf{d}$ can be expressed as

$$\langle \mathbf{d}, \hat{\mathbf{e}}_z \rangle = d\langle [\hat{\mathbf{e}}_r]_{\mathcal{F}}, \hat{\mathbf{e}}_z \rangle = d[s\beta(s\phi c\theta s\gamma - s\theta c\gamma) + c\beta c\phi c\theta] \tag{B4}$$

which (combining with Eq. (B1) and $\mu = 1/d$) yields the lower-surface nearness function for a general pose $\mathbf{q}$ of the vehicle via

$$\mu(\gamma, \beta) = \frac{\langle [\hat{\mathbf{e}}_r]_{\mathcal{F}}, \hat{\mathbf{e}}_z \rangle}{h_D - z}$$

This concept can easily be extended to a surface above the vehicle by taking

$$\mu(\gamma, \beta) = \frac{\langle [\hat{\mathbf{e}}_r]_{\mathcal{F}}, -\hat{\mathbf{e}}_z \rangle}{h_U + z}$$

For a wall to the east of the vehicle,

$$\mu(\gamma, \beta) = \frac{\langle [\hat{\mathbf{e}}_r]_{\mathcal{F}}, \hat{\mathbf{e}}_y \rangle}{a_E - y}$$

Repeating this method for west, north, and south walls, the individual μ functions can be combined to obtain a piecewise function that describes the nearness to surfaces when the vehicle is inside an enclosed rectangular prism. The resulting nearness function is then given by Eq. (4).

Table A1 MAV stability characteristics

Force/moment coefficients	Actuator dynamics coefficients
$X_u = -0.5214$	$\tau_f = 0.15$
$Y_v = -0.4799$	$\xi_\chi = 1.55$
$Z_w = -0.6802$	$\xi_{\text{lat}} = 0.245$
$Z_{\Omega_{\text{mr}}} = 0.170$	$\xi_{\text{lon}} = 0.043$
$L_v = -8.246$	$\chi_\xi = -2.82$
$L_\xi = 1273$	$\chi_{\text{lat}} = 0.044$
$M_u = 3.599$	$\chi_{\text{lon}} = -0.202$
$M_\chi = 341.6$	$T_{\Omega_{\text{mr}}} = -6.182$
$N_r = -0.8786$	$T_{\Lambda_t} = 1449$
$N_{\Lambda_y} = 39.06$	$g = 9.81$

Acknowledgments

Support for this research was provided in part by the U.S. Air Force Research Laboratory under contract FA8651-07-C-0099. The authors gratefully acknowledge Aurora Flight Sciences for creating the 3-D urban environment used herein. Thanks also to David McLaren and Bryan Patrick for developing the multipurpose

Table A2 Feedback gains

Cyclic lateral input	Cyclic longitudinal input	Main rotor input	Tail input	Reference
$K_{\Lambda_{\text{lat}},y} = 4.70$	$K_{\Lambda_{\text{lon}},y} = 0.12$	$K_{\Lambda_t,y} = -0.01$	$K_{\Lambda_{\text{yaw}},y} = 1.70$	$K_{z,\theta} = -3.50$
$K_{\Lambda_{\text{lat}},z} = 0.00$	$K_{\Lambda_{\text{lon}},z} = -0.01$	$K_{\Lambda_t,z} = -1.00$	$K_{\Lambda_{\text{yaw}},z} = 0.00$	——
$K_{\Lambda_{\text{lat}},\phi} = 11.05$	$K_{\Lambda_{\text{lon}},\phi} = 0.17$	$K_{\Lambda_t,\phi} = -0.03$	$K_{\Lambda_{\text{yaw}},\phi} = -1.78$	——
$K_{\Lambda_{\text{lat}},\theta} = 0.73$	$K_{\Lambda_{\text{lon}},\theta} = -19.02$	$K_{\Lambda_t,\theta} = 0.63$	$K_{\Lambda_{\text{yaw}},\theta} = 0.03$	——
$K_{\Lambda_{\text{lat}},\psi} = 3.42$	$K_{\Lambda_{\text{lon}},\psi} = 0.07$	$K_{\Lambda_t,\psi} = -0.01$	$K_{\Lambda_{\text{yaw}},\psi} = 2.60$	——
$K_{\Lambda_{\text{lat}},u} = -0.22$	$K_{\Lambda_{\text{lon}},u} = 8.70$	$K_{\Lambda_t,u} = -0.18$	$K_{\Lambda_{\text{yaw}},u} = 0.01$	——
$K_{\Lambda_{\text{lat}},v} = 4.35$	$K_{\Lambda_{\text{lon}},v} = 0.17$	$K_{\Lambda_t,v} = -0.01$	$K_{\Lambda_{\text{yaw}},v} = -2.01$	——
$K_{\Lambda_{\text{lat}},w} = 0.00$	$K_{\Lambda_{\text{lon}},w} = -0.06$	$K_{\Lambda_t,w} = -2.20$	$K_{\Lambda_{\text{yaw}},w} = 0.00$	——
$K_{\Lambda_{\text{lat}},p} = 0.81$	$K_{\Lambda_{\text{lon}},p} = -0.13$	$K_{\Lambda_t,p} = 0.00$	$K_{\Lambda_{\text{yaw}},p} = -0.03$	——
$K_{\Lambda_{\text{lat}},q} = -0.05$	$K_{\Lambda_{\text{lon}},q} = -1.32$	$K_{\Lambda_t,q} = -0.07$	$K_{\Lambda_{\text{yaw}},q} = 0.00$	——
$K_{\Lambda_{\text{lat}},r} = -0.03$	$K_{\Lambda_{\text{lon}},r} = 0.00$	$K_{\Lambda_t,r} = 0.00$	$K_{\Lambda_{\text{yaw}},r} = 1.09$	——
$K_{\Lambda_{\text{lat}},\xi} = 29.70$	$K_{\Lambda_{\text{lon}},\xi} = 4.35$	$K_{\Lambda_t,\xi} = 0.10$	$K_{\Lambda_{\text{yaw}},\xi} = -0.64$	——
$K_{\Lambda_{\text{lat}},\chi} = 5.49$	$K_{\Lambda_{\text{lon}},\chi} = -20.43$	$K_{\Lambda_t,\chi} = -0.48$	$K_{\Lambda_{\text{yaw}},\chi} = -0.09$	——
$K_{\Lambda_{\text{lat}},\Omega_{\text{mr}}} = 0.00$	$K_{\Lambda_{\text{lon}},\Omega_{\text{mr}}} = 0.00$	$K_{\Lambda_t,\Omega_{\text{mr}}} = 0.02$	$K_{\Lambda_{\text{yaw}},\Omega_{\text{mr}}} = 0.00$	——

simulation software AVLSim and to Joseph Conroy for the MAV system identification.

References

[1] Amidi, O., Mesaki, Y., and Kanade, T., "A Visual Odometer for Autonomous Helicopter Flight," *Robotics and Autonomous Systems*, Vol. 28, Aug. 1999, p. 185. doi:10.1016/S0921-8890(99)00016-0

[2] Gurfil, P., and Rotstein, H., "Partial Aircraft State Estimation from Visual Motion using the Subspace Constraints Approach," *Journal of Guidance, Control, and Dynamics*, Vol. 24, No. 5, 2001, pp. 1016–1028. doi:10.2514/2.4811

[3] Hrabar, S., and Sukhatme, G. S., "Omnidirectional Vision for an Autonomous Helicopter," *IEEE International Conference on Robotics and Automation '03*, IEEE Publications, Piscataway, NJ, Nov. 2003, pp. 558–563.

[4] Garratt, M., and Chahl, J., "Visual Control of an Autonomous Helicopter," 41st Aerospace Sciences Meeting and Exhibit, AIAA Paper 2003-460, 2003.

[5] Garcia-Pardo, P. J., Sukhatme, G. S., and Montgomery, J. F., "Towards Vision-Based Safe Landing for an Autonomous Helicopter," *Robotics and Autonomous Systems*, Vol. 38, No. 1, 2002, pp. 19–29. doi:10.1016/S0921-8890(01)00166-X

[6] Li, J., and Chellappa, R., "A Factorization Method for Structure from Planar Motion," *Proceedings of the IEEE Workshop on Motion and Video Computing*, Vol. 2, IEEE Publications, Piscataway, NJ, Jan. 2005, pp. 154–159. doi:10.1109/ACVMOT.2005.4

[7] Kendoula, F., Fantoni, I., and Nonamib, K., "Optic Flow-Based Vision System for Autonomous 3D Localization and Control of Small Aerial Vehicles," *Robotics and Autonomous Systems*, 2009 (in press).

[8] Frye, M. A., and Dickinson, M. H., "Fly Flight: A Model for the Neural Control of Complex Behavior," *Neuron*, Vol. 32, No. 3, 2001, pp. 385–388. doi:10.1016/S0896-6273(01)00490-1

[9] Egelhaaf, M., Kern, R., Krapp, H., Kretzberg, J., Kurtz, R., and Warzecha, A., "Neural Encoding of Behaviourally Relevant Visual-Motion Information in the Fly," *Trends in Neurosciences*, Vol. 25, No. 2, 2002, pp. 96–102. doi:10.1016/S0166-2236(02)02063-5

[10] Borst, A., and Haag, J., "Neural Networks in the Cockpit of the Fly," *Journal of Comparative Physiology A: Sensory, Neural, and Behavioral Physiology*, Vol. 188, No. 6, 2002, pp. 419–437. doi:10.1007/s00359-002-0316-8

[11] Gibson, J. J., *The Perception of the Visual World*, Houghton–Mifflin, Boston, 1950.

[12] David, C. T., "Compensation for Height in the Control of Groundspeed by Drosophila in a New, Barber's Pole Wind Tunnel," *Journal of Comparative Physiology*, Vol. 147, No. 4, 1982, pp. 485–493. doi:10.1007/BF00612014

[13] Srinivasan, M. V., Zhang, S. W., Lehrer, M., and Collett, T. S., "Honeybee Navigation En Route to the Goal: Visual Flight Control and Odometry," *Journal of Experimental Biology*, Vol. 199, No. 1, 1996, pp. 237–244.

[14] Tammero, L. F., and Dickinson, M. H., "The Influence of Visual Landscape on the Free Flight Behavior of the Fruit Fly Drosophila Melanogaster," *Journal of Experimental Biology*, Vol. 205, Feb. 2002, pp. 327–343.

[15] Hrabar, S., Sukhatme, G. S., Corke, P., Usher, K., and Roberts, J., "Combined Optic-Flow and Stereo-Based Navigation of Urban Canyons for a UAV," *Proceedings of the IEEE International Conference on Intelligent Robots and Systems*, IEEE Publications, Piscataway, NJ, Dec. 2005, pp. 3309–3316. doi:10.1109/IROS.2005.1544998

[16] Griffiths, S., Saunders, J., Curtis, A., Barber, B., McLain, T., and Beard, R., "Maximizing Miniature Aerial Vehicles: Obstacle and Terrain Avoidance for MAVs," *IEEE Robotics and Automation Magazine*, Vol. 13, No. 3, 2006, pp. 34–43. doi:10.1109/MRA.2006.1678137

[17] Muratet, L., Doncieux, S., and Meyer, J.-A., "A Biomimetic Reactive Navigation System Using the Optical Flow for a Rotary-Wing UAV in Urban Environment," *Proceedings of the 35th International Symposium of Robotics* [CD-ROM], International Symposium of Robotics, Paris, 2004.

[18] Beyeler, A., Zufferey, J.-C., and Floreano, D., "3D Vision-Based Navigation for Indoor Microflyers," *Proceedings of the 2007 IEEE International Conference on Robotics and Automation*, IEEE Publications, Piscataway, NJ, May 2007, pp. 1336-1341. doi:10.1109/ROBOT.2007.363170

[19] Griffiths, S., Saunders, J., Curtis, A., McLain, T., and Beard, R., "Obstacle and Terrain Avoidance for Miniature Aerial Vehicles," *Advances in Unmanned Aerial Vehicles*, Vol. 33, Springer, Dordrecht, The Netherlands, 2007.

[20] Chahl, J. S., and Srinivasan, M. V., "A Complete Panoramic Vision System, Incorporating Imaging, Ranging, and Three Dimensional Navigation," *Proceedings of the IEEE Workshop on Omnidirectional Vision*, IEEE Publications, Piscataway, NJ, Aug. 2002, pp. 104–111. doi:10.1109/OMNVIS.2000.853815

[21] Franceschini, N., Ruffier, F., and Serres, J., "A Bio-Inspired Flying Robot Sheds Light on Insect Piloting Abilities," *Current Biology*, Vol. 17, No. 4, 2007, pp. 329–335. doi:10.1016/j.cub.2006.12.032

[22] Beyeler, A., Zufferey, J.-C., and Floreano, D., "Optic-Flow to Steer and Avoid Collisions in 3D," *Flying Insects and Robotics*, Springer–Verlag, Berlin, 2009.

[23] Miao, A. X., Zacharias, G. L., and Warren, R., "Passive Navigation from Image Sequences: A Practitioner's Approach," AIAA Flight Simulation Technologies Conference, AIAA Paper 1996-3556, 1996.

[24] Kehoe, J. J., Watkins, A. S., Causey, R. S., and Lind, R., "State Estimation using Optical Flow from Parallax-Weighted Feature Tracking," AIAA Guidance, Navigation, and Control Conference and Exhibit, AIAA Paper 2006-6721, 2006.

[25] Bruss, A. R., and Horn, K. P., "Passive Navigation," *Computer Vision, Graphics, and Image Processing*, Vol. 21, No. 1, 1983, pp. 3–20. doi:10.1016/S0734-189X(83)80026-7

[26] Franz, M. O., Chahl, J. S., and Krapp, H. G., "Insect-Inspired Estimation of Egomotion," *Neural Computation*, Vol. 16, No. 11, 2004, pp. 2245–2260. doi:10.1162/0899766041941899

[27] Toupet, O., Paduano, J. D., Panish, R., Sedwick, R., and Frazzoli, E., "Augmenting State Estimates with Multiple Camera Visual Measurements," AIAA Infotech at Aerospace Conference and Exhibit, AIAA Paper 2007-2983, 2007.

[28] Franz, M. O., and Krapp, H. G., "Wide-Field, Motion-Sensitive Neurons and Matched Filters for Optic Flow Fields," *Biological Cybernetics*, Vol. 83, No. 3, 2000, pp. 185–197. doi:10.1007/s004220000163

[29] Grunwald, A. J., "Stability and Control of a Remotely Controlled Indoors Micro Hovering Vehicle," AIAA Guidance, Navigation, and Control Conference and Exhibit, AIAA Paper 2005-6283, 2005.

[30] Webb, T. P., Prazenica, R. J., Kurdila, A. J., and Lind, R., "Vision-Based State Estimation for Autonomous Micro Air Vehicles," *Journal of Guidance, Control, and Dynamics*, Vol. 30, No. 3, 2007, pp. 816–826. doi:10.2514/1.22398

[31] Call, B., Beard, R., and Taylor, C., "Obstacle Avoidance for Unmanned Vehicles Using Image Feature Tracking," AIAA Guidance, Navigation, and Control Conference, AIAA Paper 2006-6541, 2006.

[32] Hausen, K., "Motion Sensitive Interneurons in the Optomotor System of the Fly, Part 1: The Horizontal Cells - Structure and Signals," *Biological Cybernetics*, Vol. 45, No. 2, 1982, pp. 143–156. doi:10.1007/BF00335241

[33] Hausen, K., "Motion Sensitive Interneurons in the Optomotor System of the Fly, Part 2: The Horizontal Cells - Receptive Field Organization and Response Characteristics," *Biological Cybernetics*, Vol. 46, No. 1, 1982, pp. 67–79. doi:10.1007/BF00335352

[34] Hengstenberg, R., Hausen, K., and Hengstenberg, B., "The Number and Structure of Giant Vertical Cells (VS) in the Lobula Plate of the Blowfly Calliphora Erythrocephala," *Journal of Comparative Physiology*, Vol. 149, No. 2, 1982, pp. 163–177. doi:10.1007/BF00619211

[35] Humbert, J. S., and Hyslop, A. M., "Bio-Inspired Visuomotor Convergence," *IEEE Transactions on Robotics and Automation*, 2009 (in press).

[36] Srinivasan, M. V., Zhang, S., and Chahl, J. S., "Landing Strategies in Honeybees, and Possible Applications to Autonomous Airborne Vehicles," *The Biological Bulletin*, Vol. 200, April 2001, pp. 216–221. doi:10.2307/1543319

[37] Humbert, J. S., Murray, R. M., and Dickinson, M. H., "Sensorimotor Convergence in Visual Navigation and Flight Control Systems," *Proceedings of the 16th IFAC World Congress* [CD-ROM], Elsevier, New York, June 2005.

[38] Humbert, J. S., Murray, R. M., and Dickinson, M. H., "Pitch-Altitude Control and Terrain Following Based on Bio-Inspired Visuomotor Convergence," AIAA Guidance, Navigation, and Control Conference, AIAA Paper 2005-6280, 2005.

[39] Humbert, J. S., Murray, R. M., and Dickinson, M. H., "A Control-Oriented Analysis of Bio-Inspired Visuomotor Convergence," *Proceedings of the 44th IEEE Conference on Decision and Control*, IEEE Publications, Piscataway, NJ, Jan. 2006, pp. 245–250.

[40] Xu, P., Humbert, J. S., and Abshire, P., "Implementation and Demonstration of Wide-Field Integration in Analog VLSI," *IEEE Transactions on Control Systems Technology*, 2009 (submitted for publication).

[41] Koenderink, J. J., and van Doorn, A. J., "Facts on Optic Flow," *Biological Cybernetics*, Vol. 56, No. 4, 1987, pp. 247–254. doi:10.1007/BF00365219

[42] Egelhaaf, M., and Borst, A., "Motion Computation and Visual Orientation in Flies," *Comparative Biochemistry Physiology*, Vol. 104, No. 4, 1993, pp. 659–673. doi:10.1016/0300-9629(93)90144-S

[43] Krapp, H. G., Hengstenberg, B., and Hengstenberg, R., "Dendritic Structure and Receptive-Field Organization of Optic Flow Processing Interneurons in the Fly," *Journal of Neurophysiology*, Vol. 79, No. 4, 1998, pp. 1902–1917.

[44] Conroy, J. K., Humbert, J. S., and Pines, D., "System Identification of a Rotary-Wing Micro Air Vehicle," *Journal of the American Helicopter Society*, 2009 (accepted for publication).

[45] Kwakernaak, H., and Sivan, R., *Linear Optimal Control Systems*, 1st ed., Wiley–Interscience, New York, 1972.

[46] Zufferey, J. C., and Floreano, D., "Fly-Inspired Visual Steering of an Ultralight Indoor Aircraft," *IEEE Transactions on Robotics and Automation*, Vol. 22, No. 1, 2006, pp. 137–146. doi:10.1109/TRO.2005.858857

[47] Shi, R. Z., and Horiuchi, T. K., "A Neuromorphic VLSI Model of Bat Interaural Level Difference Processing for Azimuthal Echolocation," *IEEE Transactions on Circuits and Systems 1: Regular Papers*, Vol. 54, No. 1, 2007, pp. 74–88. doi:10.1109/TCSI.2006.887981

[48] Chao, H., Cao, Y., and Chen, Y., "Autopilots for Small Fixed-Wing Unmanned Air Vehicles: A Survey," *Proceedings of the IEEE International Conference on Mechatronics and Automation*, IEEE Publications, Piscataway, NJ, Sept. 2007, pp. 3144–3149. doi:10.1109/ICMA.2007.4304064

[49] Conroy, J. K., Gremillion, G., Ranganathan, B., and Humbert, J. S., "Implementation of Wide-Field Integration Methods for Autonomous Micro Helicopter Navigation," *Autonomous Robots*, 2009 (accepted for publication).

[50] Hrabar, S., and Sukhatme, G. S., "A Comparison of Two Camera Configurations for Optic-Flow Based Navigation of a UAV Through Urban Canyons," *Proceedings of the IEEE International Conference on Intelligent Robots and Systems*, Vol. 3, IEEE Publications, Piscataway, NJ, Feb. 2004, pp. 2673–2680. doi:10.1109/IROS.2004.1389812

[51] Humbert, J. S., Hyslop, A., and Chinn, M., "Experimental Validation of Wide-Field Integration Methods for Autonomous Navigation," *Proceedings of IEEE/RSJ International Conference on Intelligent Robots and Systems*, IEEE Publications, Piscataway, NJ, Dec. 2007, pp. 2144–2149. doi:10.1109/IROS.2007.4399488

[52] Hyslop, A. M., and Humbert, J. S., "Wide-Field Integration Methods for Autonomous Navigation of 3-D Environments," AIAA Guidance, Navigation, and Control Conference, AIAA Paper 2008-7252, 2008.

[53] DeSouza, G. N., and Kak, A. C., "Vision for Mobile Robot Navigation: A Survey," *IEEE Transactions on Pattern Analysis and Machine Intelligence*, Vol. 24, No. 2, 2002, pp. 237–266. doi:10.1109/34.982903